

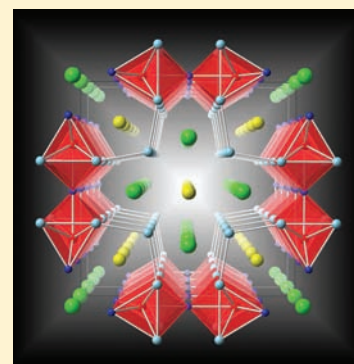
Synthesis and Properties of New Multinary Silicides $R_5Mg_5Fe_4Al_xSi_{18-x}$ ($R = Gd, Dy, Y, x \approx 12$) Grown in Mg/Al Flux

Xiaowei Ma, Banghao Chen, and Susan E. Latturmer*

Department of Chemistry and Biochemistry, Florida State University, Tallahassee, Florida 32306, United States

Supporting Information

ABSTRACT: Reactions of iron, silicon, and $R = Gd, Dy, \text{ or } Y$ in 1:1 Mg/Al mixed flux produce well-formed crystals of $R_5Mg_5Fe_4Al_xSi_{18-x}$ ($x \approx 12$). These phases have a new structure type in tetragonal space group $P4/mmm$ ($a = 11.655(2) \text{ \AA}$, $c = 4.0668(8) \text{ \AA}$, $Z = 1$ and $R_1 = 0.0155$ for the Dy analogue). The structure features two rare earth sites and one iron site; the latter is in monocapped trigonal prismatic coordination surrounded by silicon and aluminum atoms. Siting of Al and Si was investigated using bond length analysis and ^{27}Al and ^{29}Si MAS NMR studies. The magnetic properties are determined by the R elements, with the Gd and Dy analogues exhibiting antiferromagnetic ordering at $T_N = 11.9$ and 6.9 K respectively; both phases exhibit complex metamagnetic behavior with varying field.



INTRODUCTION

Intermetallic silicides are of interest for a wide variety of applications. Thin films of refractory phases such as $TiSi_2$ and $CoSi_2$ are used as diffusion barriers in microelectronics, facilitated by their excellent bonding to silicon.¹ Many transition metal silicides have interesting magnetic or transport properties; Fe_3Si is a ferromagnetic metal, while $FeSi_2$ is a small bandgap semiconductor of interest as a thermoelectric material.^{2,3} Silicon is often added to metal alloys to strengthen them, causing precipitation hardening from formation of adventitious secondary silicide phases, such as microcrystals of $CaMgSi$ in magnesium alloys and $Al_{12}Mn_3Si_2$, Al_8Fe_2Si , and the “ π -phase” $Al_5FeMg_3Si_5$ in aluminum alloys.^{4–7} Gaining an understanding of the formation and structure of these precipitates will give metallurgists increased ability to control the properties of important alloys.

We have been investigating the synthesis of silicides in Mg/Al flux. Metal flux chemistry allows for dissolution of refractory elements, lower reaction temperatures, and crystal growth. This synthesis technique has enabled the discovery of new phases Eu_2AuGe_3 and $Li_2B_{12}Si_2$ (from reactions in indium and tin fluxes respectively) and more complete characterization of known phases such as $Ba_8Al_{16}Si_{30}$ (grown in Al flux).^{8–10} Using a mixture of two metals as a flux can further this technique by lowering the solvent melting point through eutectic formation and increasing the range of elements soluble in the flux. In recent years we have explored La/Ni eutectics for growth of magnetic phases such as $La_{21}Fe_8Sn_7C_{12}$ and $La_6Fe_{10}Al_3Sb$, and Ca/Li mixtures for growth of new carbides and hydrides such as $LiCa_2C_3H$ and $LiCa_7Ge_3H_3$.^{11–13} We have also found that Mg/Al mixtures are particularly good solvents for the formation of silicides, allowing for growth of large crystals of $CaMgSi$ and other phases.¹⁴

The Mg/Al phase diagram contains a wide low melting range between 40–60% Mg, and only two known binary phases, Mg_2Al_3 and $Mg_{17}Al_{12}$.¹⁵ A 1:1 mixture of Mg/Al melts at 460 °C. Reactions of silicon, iron, and $R = Gd, Dy, \text{ or } Y$ in this flux produce crystals of $R_5Mg_5Fe_4Al_xSi_{18-x}$ ($x \approx 12$). This phase has a complex structure stemming from the presence of several elements which prefer very different coordination environments. The rare earth elements occupy two distinct crystallographic sites and determine the magnetic properties of the compound. These phases were studied by single crystal X-ray and solid state NMR, and the antiferromagnetic ordering observed in the Dy and Gd analogues were characterized with susceptibility measurements.

EXPERIMENTAL PROCEDURES

Synthesis. Mg and Al metal slugs (99.95%) and Fe powder (99+%) were obtained from Alfa Aesar. Si (99+%) and Y(99.9%) powders were obtained from Strem Chemicals. Gd and Dy powders (99.9%) were obtained from Metall. The elements Mg/Al/Si/Fe/(Gd, Dy, or Y) were initially weighed out in a 15/15/2/1/1 mmol ratio and loaded into stainless steel crucibles in a drybox. The steel crucibles were welded shut in an argon-filled glovebox and then sealed into fused silica tubes under vacuum. All reaction ampules were placed in a muffle furnace and heated from room temperature to 950 °C in 10 h, held at 950 °C for 5 h, cooled to 750 °C in 80 h, and held at 750 °C for 24 h, at which point the reaction ampules were quickly removed from the furnace, flipped, and centrifuged to let the excess Mg/Al molten flux decant off the product crystals which adhered to the crucible walls. Several reactions were run to determine the optimal reactant ratios; after these were determined, crystals were grown with the optimal mmol ratio of elements in niobium crucibles to eliminate incorporation of impurities.

Received: December 20, 2011

Published: May 16, 2012

Elemental Analysis. SEM-EDS analysis was performed using a JEOL 5900 scanning electron microscope (30 kV acceleration voltage) equipped with PGT Prism energy dispersion spectroscopy software. Selected crystals were arranged on double-sided carbon tape adhered to an aluminum sample puck. Each crystal was cleaved to expose inner portions to acquire more accurate elemental analysis of the bulk sample and avoid erroneous readings caused by residual flux coating on the surface. Several spots on each crystal were analyzed for 60 s at each location. Aluminum and silicon pieces were used as external standards to improve the quantification of these elements (see Supporting Information, Table S1).

X-ray Diffraction. Single crystal diffraction data were collected for each analogue at room temperature on a Bruker APEX2 single crystal diffractometer with a Mo $K\alpha$ radiation source. Selected crystal samples were broken into suitable size and small spheroid fragments were mounted on glass fibers for diffraction. Data was processed using the program SAINT and corrected with the SADABS program.¹⁶ Space group assignment was accomplished by XPREP, and refinement of the structure was performed by SHELXTL.¹⁷ The structures were solved in tetragonal space group $P4/mmm$; crystallographic data and

Table 1. Crystallographic Data and Collection Parameters for $R_5Mg_5Fe_4Al_{12}Si_6$ Phases

	$Gd_5Mg_5Fe_4Al_{12}Si_6$	$Dy_5Mg_5Fe_4Al_{12}Si_6$	$Y_5Mg_5Fe_4Al_{12}Si_6$
crystal system	tetragonal	tetragonal	tetragonal
space group	$P4/mmm$	$P4/mmm$	$P4/mmm$
cell param, Å	$a = 11.707(4)$ $c = 4.087(1)$	$a = 11.655(2)$ $c = 4.0668(8)$	$a = 11.703(11)$ $c = 4.074(4)$
$V, \text{Å}^3$	560.2(4)	552.5(2)	558.0(9)
Z	1	1	1
calc. density (g/cm^3)	4.81	4.96	3.82
2θ (max)	56.26	56.10	56.25
radiation	Mo $K\alpha$	Mo $K\alpha$	Mo $K\alpha$
temperature (K)	290	290	290
reflections	6313	6204	5362
unique reflections	450	428	446
data/parameters	450/35	428/35	446/35
μ (mm^{-1})	18.01	20.16	16.29
$R(\text{int})$	0.0292	0.0289	0.0336
R_1/wR_2^a ($I > 2\sigma(I)$)	0.0138/0.0333	0.0155/0.0385	0.0229/0.0563
R_1/wR_2 (all data)	0.0148/0.0335	0.0158/0.0386	0.0244/0.0567
largest diff peak and hole ($e\text{-Å}^{-3}$)	0.64/−0.76	1.49/−0.87	1.18/−0.72

$$^a R_1 = \frac{\sum ||F_o| - |F_c||}{\sum |F_o|}; wR_2 = \left[\frac{\sum w(F_o^2 - F_c^2)^2}{\sum w(F_o^2)^2} \right]^{1/2}$$

collection parameters are shown in Tables 1 and 2; further data can be found in the Supporting Information, Table S2 and CIF files. During the refinement, assignment of rare earth and iron sites were straightforward; all lighter element sites (Mg, Al, Si) were initially assigned as aluminum, but assignments were modified based on bond length considerations, elemental analysis, and NMR data (see discussion). Allowing the occupancies of these light element sites to vary was not informative (because of very similar X-ray scattering factors, the Al and Si sites appeared fully occupied whether assigned as Al or Si). In the final refinement cycles, occupancies of all sites were allowed to vary, but all appeared fully occupied ($100 \pm 1\%$). Powder X-ray diffraction data were collected for each analogue on a PANalytical X'Pert PRO with a Cu $K\alpha$ radiation source.

Magnetic Susceptibility. Magnetic susceptibility measurements were carried out on a Quantum Design SQUID Magnetic Property Measurement System. Crystals grown in Nb crucibles were selected

Table 2. Atom Positions and Isotropic Thermal Parameters for $Dy_5Mg_5Fe_4Al_{12}Si_6$

	Wyckoff Site	x	y	z	U_{eq}^a
Dy1	$4n$	0.26556(2)	1/2	0	0.0073(1)
Dy2	$1a$	0	0	0	0.0130(2)
Mg1	$4j$	0.2022(1)	0.2022(1)	0	0.0086(4)
Mg2	$1d$	1/2	1/2	1/2	0.0111(9)
Fe1	$4l$	0.29640(9)	0	0	0.0103(2)
Al1	$8q$	0.1157(1)	0.3703(1)	1/2	0.0085(3)
Al2	$4k$	0.3315(1)	0.3315(1)	1/2	0.0030(4)
Si1	$4m$	0.1793(1)	0	1/2	0.0118(4)
Si2	$2f$	0	1/2	0	0.0128(5)

^a U_{eq} is defined as one-third of the trace of the orthogonalized U_{ij} tensor.

and held between two strips of kapton tape. Temperature-dependent susceptibility data were collected between 1.8 K and 300 K at 100 G for the dysprosium phase and 100 to 30000 G for the gadolinium and yttrium analogues. Field-dependent data were collected at 1.8 K using fields up to 7 T; crystals were oriented with c -axis parallel to the applied field.

Solid State NMR Characterization. ²⁷Al and ²⁹Si MAS NMR spectra were collected on a Varian/Inova 500WB spectrometer (11.7 T) with resonance frequencies of 130.46 and 99.40 MHz respectively. The ²⁷Al and ²⁹Si shifts were referenced to 1 M Al(NO₃)₃ and TMS. Crystals of $Y_5Mg_5Fe_4Al_xSi_{18-x}$ were ground with NaCl in a 1:1 ratio by volume in a glovebox, and the powder was packed into a 4 mm zirconia rotor sealed with airtight screw caps. The ²⁹Si MAS spectra were obtained with a spinning speed of 13 kHz and a recycle delay of 60 s. For the ²⁷Al MAS experiment, single pulse acquisition was applied with a short RF pulse less than 15°. The spinning speed was 12 kHz and the recycle delay was 0.3 s.

RESULTS AND DISCUSSION

Synthesis. The $R_5Mg_5Fe_4Al_xSi_{18-x}$ phases were synthesized in excess Mg/Al flux in steel crucibles. The optimal Mg/Al/Si/Fe/R reactant ratio is 15:15:3:1:2 for R = Gd, 15:15:2:0.5:1 for R = Dy, and 15:15:4:1:2 for R = Y (in each case the yield was 90% or higher based on Fe). Products formed as silver needles up to 4 mm in length and 1 mm in diameter as shown in Figure 1; small amounts of silver/gray powder were also present. Visual inspection and powder diffraction data (see Supporting Information, Figure S1) do not indicate the presence of significant amounts of byproducts in the Gd and Dy syntheses, although the $Y_5Mg_5Fe_4Al_xSi_{18-x}$ powder pattern does show some small peaks corresponding to trace amounts of YFe_4Al_8 ,

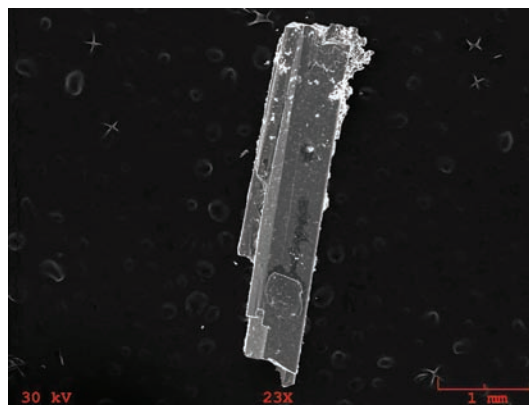


Figure 1. SEM image of a crystal of $Gd_5Mg_5Fe_4Al_{12}Si_6$.

Fe_2Al_5 , Y_5Si_3 , and Mg_2Si (the first two compounds may contribute to the ferromagnetism observed in the magnetic susceptibility data, *vide infra*). Some crystals had traces of flux residue on their surfaces. Semiquantitative elemental analysis by SEM-EDS did not indicate incorporation of contaminant elements from the steel crucible, although traces of contamination cannot be ruled out (magnetic measurements were carried out on products grown in niobium crucibles). The products are stable to air and water but dissolve slowly in 5 M HNO_3 . This structure forms with $R = \text{Gd}, \text{Dy}, \text{Y}$; attempts to synthesize analogues with early rare earths (La–Eu) or late rare earths (Er–Lu) led to different phases, as did attempts to replace Si with Ge. It is notable that the combination of this many elements yields the quinary title compounds instead of known ternaries such as REFe_4Al_8 ($\text{RE} = \text{Gd}, \text{Dy}$) and $\text{RE}_2\text{Al}_3\text{Si}_2$ ($\text{RE} = \text{Tb–Lu}, \text{Y}$) or quaternary phases such as $\text{REFe}_4\text{Al}_9\text{Si}_6$ ($\text{RE} = \text{Tb}, \text{Er}$) and $\text{Al}_9\text{FeMg}_3\text{Si}_5$.^{18–21} The presence of a large amount of magnesium in the flux likely eliminates formation of most of these potential byproducts.

Structure. $\text{R}_5\text{Mg}_5\text{Fe}_4\text{Al}_x\text{Si}_{18-x}$ exhibits a complex new structure type in tetragonal space group $P4/mmm$, shown in Figure 2. A major building block is the ribbon running in the c -

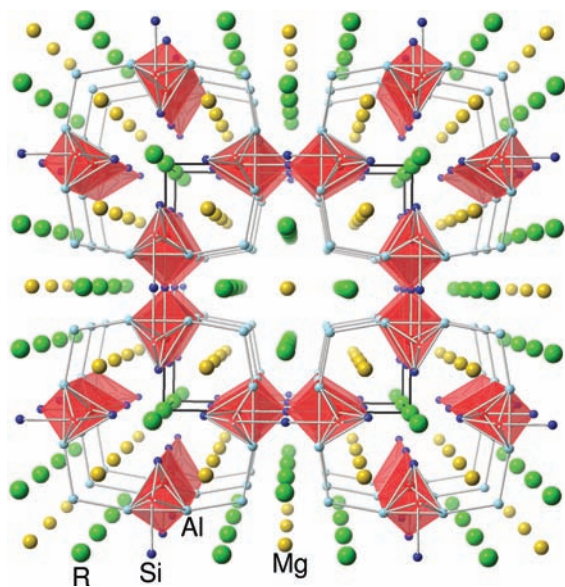


Figure 2. Structure of $\text{R}_5\text{Mg}_5\text{Fe}_4\text{Al}_{12}\text{Si}_6$, viewed down the c -axis. Ribbons of iron-centered trigonal prisms running along the c -axis are highlighted in polyhedral mode (red). Bonds to Mg and R atoms are omitted for clarity.

direction composed of iron in a monocapped trigonal prismatic coordination of Al and Si atoms, linked by the monocapping silicon atom along the a - or b -direction, and by sharing trigonal faces along the c -axis. The coordination of the iron site can also be viewed as a tricapped trigonal prism if the two neighboring Mg atoms are taken into account (Figure 3). Similar tricapped trigonal prismatic coordination of iron can be seen in the π -phase $\text{Al}_9\text{FeMg}_3\text{Si}_5$ and in RFe_2Al_8 ($R = \text{Ce}, \text{Eu}$), with the latter also featuring chains of prisms sharing trigonal faces running along one crystallographic axis.^{18,21} The bond lengths from the iron site in $\text{Dy}_5\text{Mg}_5\text{Fe}_4\text{Al}_x\text{Si}_{18-x}$ to the surrounding Al and Si atoms are all within the range of 2.37 to 2.59 Å; bonds to the Mg sites are 2.600(1) Å (see Table 3). The iron sites are fairly isolated from each other, which may be the reason for their lack of magnetic moment (*vide infra*); the iron–iron distance along

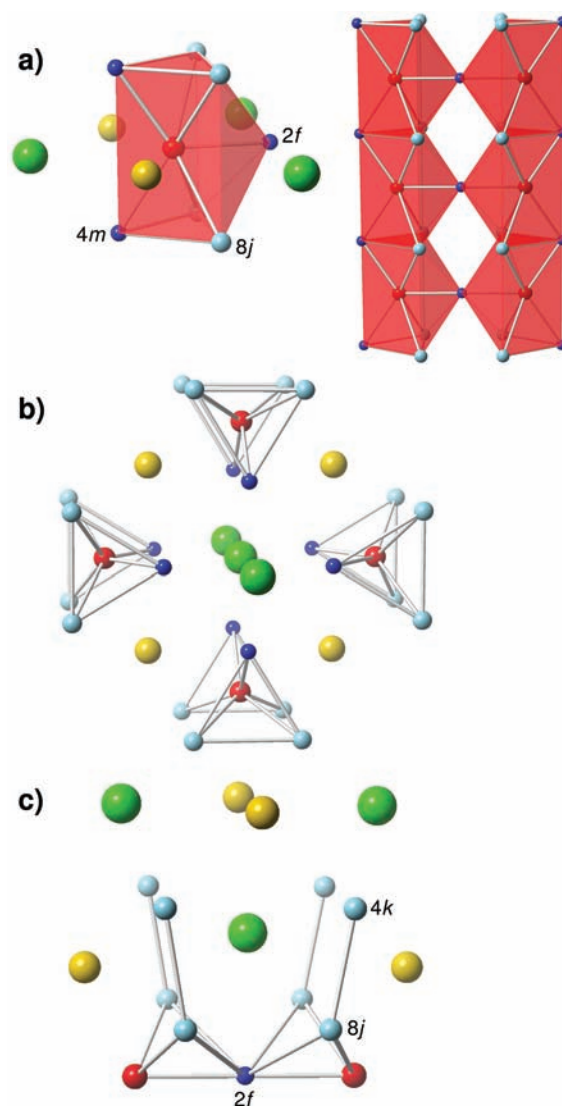


Figure 3. Coordination environments in the $\text{R}_5\text{Mg}_5\text{Fe}_4\text{Al}_{12}\text{Si}_6$ structure. Aluminum and silicon atoms are light blue and dark blue respectively. (a) Monocapped trigonal prismatic coordination of iron which share trigonal faces to form chains. (b) Coordination of the rare earth ion in the $1a$ Wyckoff site; these sites form a chain along the c -axis. (c) Coordination of the rare earth ion in the $4n$ site.

the c -axis is the length of the c -axis parameter (4.0668(8) Å for the Dy analogue) and 4.75 Å across the bridging silicon atom in the a - b plane.

The structure has two rare earth sites; one is located at the corner of the unit cell ($1a$ Wyckoff site), and the other occupies a lower symmetry site ($4n$ Wyckoff site) toward the center of the unit cell. As shown in Figure 3b, the $1a$ rare earth site is surrounded by 8 silicon atoms in a cubic coordination environment at a distance of 2.916(1) Å (for Dy phase). Four magnesium atoms are located a further distance away (3.333(2) Å). The $1a$ sites are separated from adjacent $1a$ sites by the length of the c -axis, producing a chain of rare earth atoms with R^{3+} – R^{3+} distances of around 4 Å (4.0668(8) Å for the Dy analogue). The $4n$ rare earth sites are also separated from neighboring $4n$ sites by this same distance along c , but additional symmetry equivalents are found at shorter distances in the ab -plane (3.864 Å for the Dy analogue; see Figure 3c) which may lead to complex magnetic behavior. This rare earth

Table 3. Bond Lengths in $\text{Dy}_5\text{Mg}_5\text{Fe}_4\text{Al}_{12}\text{Si}_6$

bond	bond distance, Å
Dy(1)–Al(1) ×4	3.078(1)
Dy(1)–Al(2) ×4	2.9296(7)
Dy(1)–Mg(1)	3.548(2)
Dy(1)–Mg(2) ×2	3.4060(5)
Dy(2)–Si(1) ×8	2.916(1)
Dy(2)–Mg(1) ×4	3.333(2)
Dy(2)–Fe(1)	3.455(1)
Fe(1)–Al(1) ×4	2.587(1)
Fe(1)–Si(1) ×2	2.449(1)
Fe(1)–Si(2)	2.373(1)
Fe(1)–Mg(1) ×2	2.600(1)
Mg(1)–Al(1) ×4	2.998(1)
Mg(1)–Si(1) ×4	3.125(1)
Mg(1)–Al(2) ×2	2.945(2)
Mg(2)–Al(2) ×4	2.778(2)
Al(1)–Al(1)	2.696(3)
Al(1)–Si(1)	2.602(2)
Al(1)–Al(2) ×2	2.556(2)
Al(1)–Si(2) ×2	2.870(1)

site is coordinated by 9 Al or Si atoms at distances from 2.93–3.10 Å; magnesium and iron atoms are found further away.

The major difficulty in determining the structure of this phase by X-ray diffraction is the similar numbers of electrons in Mg, Al, and Si and their resulting similar X-ray scattering factors. Magnesium sites can be located by consideration of bond lengths; Mg coordination tends to feature distinctly longer bond lengths than Al or Si. With this guideline, comparison to bond lengths reported in literature, and correlation with EDS analysis, the $4j$ and $1d$ sites were assigned as magnesium. Distinguishing between aluminum and silicon is less straightforward, as their average bond length ranges overlap; for instance, Fe–Si bonds in intermetallics generally range between 2.27 to 2.55 Å, and Fe–Al bonds between 2.42 and 2.88 Å.²² However, bond length analysis has been used for determination of Al and Si siting in phases such as $\pi\text{-Al}_9\text{FeMg}_3\text{Si}_5$ and $\alpha\text{-AlFeSi}$.^{21,22}

The elemental analyses of the title phases (see Supporting Information, Table S1) consistently indicate a 2:1 mol ratio of aluminum to silicon, supporting a stoichiometry of $\text{R}_5\text{Mg}_5\text{Fe}_4\text{Al}_{12}\text{Si}_6$. The Al/Si ratio in the product does not change significantly if the rare earth element or the amount of silicon used in the reaction is varied. X-ray data collected on products of varying reaction stoichiometries showed consistent unit cell parameters (± 0.01 Å), indicating that this phase may have a very narrow phase width. Considering the Dy analogue as an example, a short bond (2.373(1) Å) between iron and a light atom on a $2f$ Wyckoff site indicates that silicon is most likely to occupy this location (Si(2) is the monocoordinating atom that bridges two iron-centered monocoordinated trigonal prisms). The distances from the iron atoms to the adjacent $4m$ site are also short (2.450(1) Å). While this distance is in the overlapping region of the Fe–Si and Fe–Al bond length ranges, it is notable that this $4m$ site is 2.916(1) Å from a Dy^{3+} ion. The smaller, more electronegative silicon is therefore more likely to occupy this site than aluminum, and it is therefore assigned as Si(1). The $8q$ Wyckoff site is occupied by a light atom exhibiting longer bonds to iron (2.5874(9) Å), Mg (2.999(1) Å) and Dy (3.078(1) Å) and was therefore assigned as aluminum Al(1). Assignment of the remaining light atom site

(on a $4k$ site) is less clear-cut. The bond lengths to neighboring atoms are somewhat short (2.9296(6) Å to Dy^{3+} , 2.778(2) Å to Mg^{2+} , 2.556(2) Å to Al(1)), and this site is predominantly surrounded by highly electropositive species (Dy^{3+} and Mg^{2+}); both these factors would support assignment of this site as silicon which would lead to an overall stoichiometry of $\text{Dy}_5\text{Mg}_5\text{Fe}_4\text{Al}_8\text{Si}_{10}$. However, the elemental analysis data indicates that this compound is more aluminum-rich, so this $4k$ site was assigned as Al(2). It is notable that the thermal parameters of the $4m$ and $2f$ sites (both assigned as silicon) are similar to each other and differ slightly from the thermal parameters of the $8q$ and $4k$ sites assigned as aluminum; this is observed for all three analogues (Table 2; Supporting Information, Table S2). However, these assignments cannot be resolved or verified by X-ray diffraction (all occupancies were allowed to refine but did not vary from unity, and interchanging Al and Si assignments has no effect on the refinement R-values) and the possibility of site mixing also cannot be ignored.

²⁷Al and ²⁹Si solid state NMR studies were carried out to clarify the issue of possible Al/Si mixing, and also to gain insight on the electronic properties of these phases. $\text{Y}_5\text{Mg}_5\text{Fe}_4\text{Al}_{12}\text{Si}_6$ was used for these experiments to avoid any additional shifts caused by localized f -electrons in Gd or Dy. Nuclear resonances in metallic compounds are affected by the presence of conduction electrons; these produce an additional field on the nucleus and result in a Knight shift, the size of which depends on the contribution of the atom of interest to the density of states at E_F . Referenced to $\text{Al}(\text{H}_2\text{O})_6^{3+}$ at 0 ppm, pure aluminum metal exhibits a resonance at 1640 ppm, and aluminum in alloys and intermetallics typically have resonances in the 600–1700 ppm range (for instance, 1486 ppm for CuAl_2 , and 880 ppm for AlB_2).^{23–25} The “semiconducting region” for aluminum is around 100–500 ppm; aluminum in charge-balanced Zintl phases and III–V semiconductors have resonances in that range (for instance, the Zintl phase $\text{Ba}_7\text{Al}_{10}$ has resonances at 490 and 660 ppm; AlAs and AlP at 130 ppm and 142 ppm, respectively; and Al_4C_3 at 120 ppm).^{26–28} The “insulating region” for aluminum in oxides or aqueous solutions is 0–100 ppm, with AlO_4 tetrahedral units having resonances around 60 ppm and octahedral AlO_6 species having resonances near 0 ppm.²⁹

The ²⁷Al MAS NMR spectrum of $\text{Y}_5\text{Mg}_5\text{Fe}_4\text{Al}_{12}\text{Si}_6$ (Figure 4) features a narrow peak at 200 ppm and a broader peak at 1300 ppm (small peaks in the 0–100 ppm region are caused by surface oxidation). This indicates the presence of at least two aluminum sites, supporting the assignment of $8q$ and $4k$ sites as aluminum. The peak at 1300 ppm in the ²⁷Al spectrum of $\text{Y}_5\text{Mg}_5\text{Fe}_4\text{Al}_{12}\text{Si}_6$ is assigned to the $8q$ site. The broadness of this peak was not changed by higher spinning speeds. This may indicate that all the sites contain mixtures of Al and Si, so in some unit cells the $8q$ site is bonded to 2Al and 1Si, in other unit cells it is bonded to 1Al and 2Si, yielding a distribution of local environments which cannot be narrowed by magic angle spinning. Aluminum atoms mixing on the $4m$ and $2f$ sites may also contribute to this broad peak; these sites are bound to iron and other Al/Si sites would likely have similar resonances as the $8q$ site Al atoms.

The 200 ppm resonance is in the semiconducting region and will be associated with aluminum atoms with a large degree of ionic character, which corresponds to the $4k$ site. This site is surrounded by highly electropositive elements (Mg and Y), and atoms in this location should have similar electronic character-

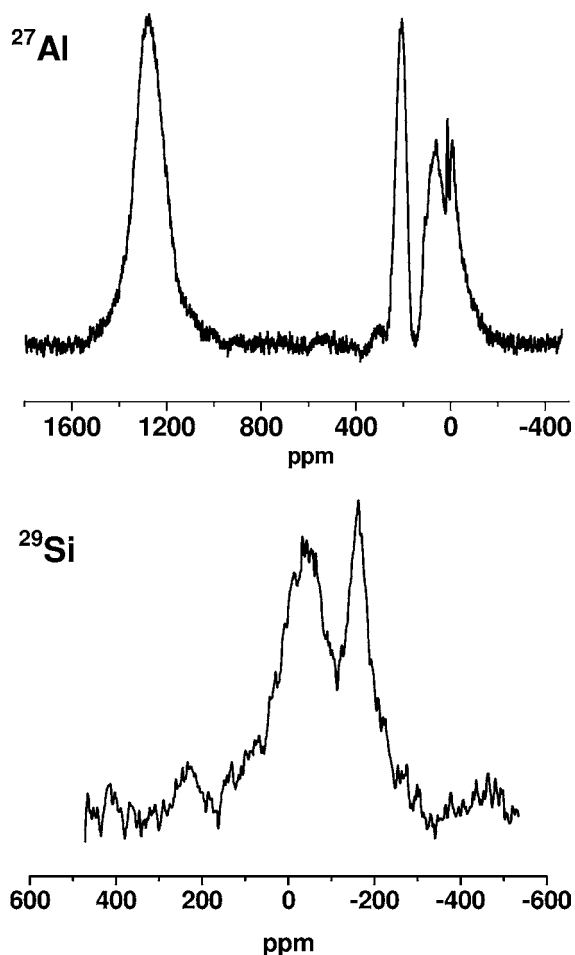


Figure 4. ^{27}Al and ^{29}Si MAS NMR spectra of $\text{Y}_5\text{Mg}_5\text{Fe}_4\text{Al}_{12}\text{Si}_6$.

istics to those in charge-balanced Zintl phases. ^{27}Al MAS NMR studies reported for the clathrate $\text{Ba}_8\text{Al}_{16}\text{Si}_{30}$ show a resonance in the metallic region (1600 ppm) and a couple in the semiconducting region (500 ppm).³⁰ This compound is metallic, but it is close to being a charge-balanced semiconductor since its structure can be viewed by Zintl phase analysis as $(\text{Ba}^{2+})_8(\text{Al}^-)_{16}(\text{Si}^0)_{30}$. The germanium analogue of this clathrate, $\text{Ba}_8\text{Al}_{16}\text{Ge}_{30}$, is even closer to being a semiconductor and its ^{27}Al resonances are in the 200 ppm region (and they exhibit broad peaks because of disorder in the Al/Ge framework).³¹

The very low ^{27}Al Knight shift of 200 ppm for the 4k site may indicate that this compound is a poor metal. This is also supported by the ^{29}Si MAS NMR data shown in Figure 4. While the resonances are unfortunately extremely broad and signal-to-noise is low, two broad peaks are seen at -50 ppm and -150 ppm with respect to TMS at 0 ppm. Silicon Knight shifts in metallic compounds are typically found in the 200 to 1000 ppm range (as observed for the silicon sites in metallic clathrates such as $\text{Na}_{24}\text{Si}_{136}$).³² The negative resonances seen for $\text{Y}_5\text{Mg}_5\text{Fe}_4\text{Al}_{12}\text{Si}_6$ are in the range characteristic of elemental semiconducting silicon (-81 ppm) and of anionic silicon in semiconductors such as the Zintl phases LiSi (-107 ppm) and Rb_4Si_4 (-290 ppm).^{32,33} The ^{27}Al and ^{29}Si NMR spectra indicate that $\text{Y}_5\text{Mg}_5\text{Fe}_4\text{Al}_{12}\text{Si}_6$ is likely a poor metal with a small density of states at E_f (with states contributed by the 8q Al site); the other Al and Si sites in the structure are somewhat anionic, contributing to bands well below E_f and resulting in

chemical shifts for these sites that are typical of these elements in semiconducting Zintl phases.

Magnetic Behavior. The magnetic characterization of these phases was hindered by incorporation of ferromagnetic impurities. The possibility of impurities from the steel crucible was eliminated by using only samples synthesized in niobium ampules for magnetic measurements. However, residual iron powder reactant or traces of ferromagnetic byproducts may also act as contaminants. Susceptibility data for both the Y and Gd analogues showed a broad ferromagnetic transition at around 100 K. However, data taken at higher fields to saturate impurities eliminated this peak. The resulting high field susceptibility data for $\text{Y}_5\text{Mg}_5\text{Fe}_4\text{Al}_{12}\text{Si}_6$ (Figure 5) is very

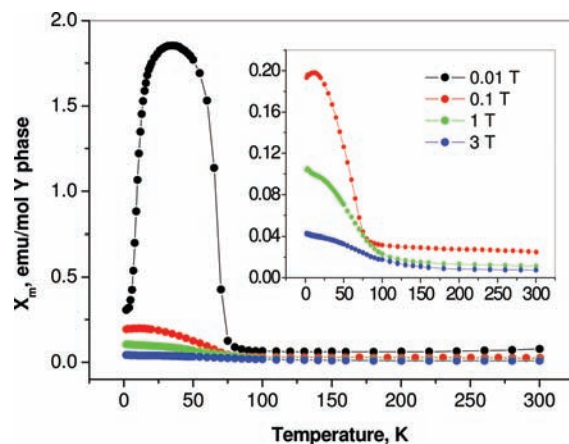


Figure 5. Temperature dependence of magnetic susceptibility of $\text{Y}_5\text{Mg}_5\text{Fe}_4\text{Al}_{12}\text{Si}_6$ at different magnetic fields.

close to temperature independent, indicating that this compound is Pauli paramagnetic, with χ_p of approximately 0.01 emu/mol (or 5×10^{-6} emu/g, a value of the magnitude expected for metals).³⁴ Therefore, the iron in this compound does not appear to have a magnetic moment.

The magnetic susceptibility data for the Gd and Dy analogues indicates that the iron in these phases is also diamagnetic, with all of the magnetic moment and ordering resulting from the rare earth ions. After correcting for a small amount of ferromagnetic impurity, the high temperature data for the $\text{Gd}_5\text{Mg}_5\text{Fe}_4\text{Al}_{12}\text{Si}_6$ phase (see Figure 6) can be fit to the Curie–Weiss law, resulting in an effective moment per Gd^{3+} ion of $8.5 \mu_B$, similar to the theoretical value of $7.94 \mu_B$.³⁴ The

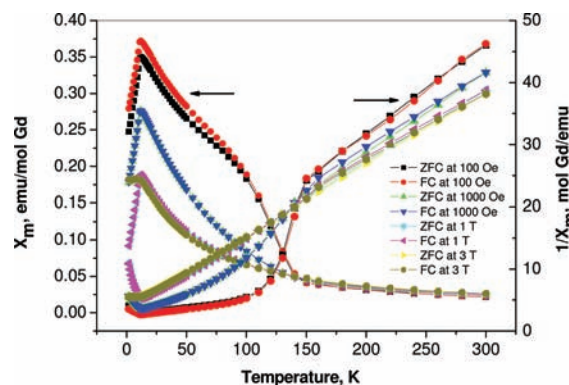


Figure 6. Temperature dependence of magnetic susceptibility of $\text{Gd}_5\text{Mg}_5\text{Fe}_4\text{Al}_{12}\text{Si}_6$ at different magnetic fields.

Weiss constant θ is -40 K, indicative of antiferromagnetic coupling forces between the Gd ions. This is in agreement with the observed antiferromagnetic ordering transition observed at $T_N = 11$ K. Field-dependent magnetization data taken at several temperatures (Figure 7) shows paramagnetic behavior above

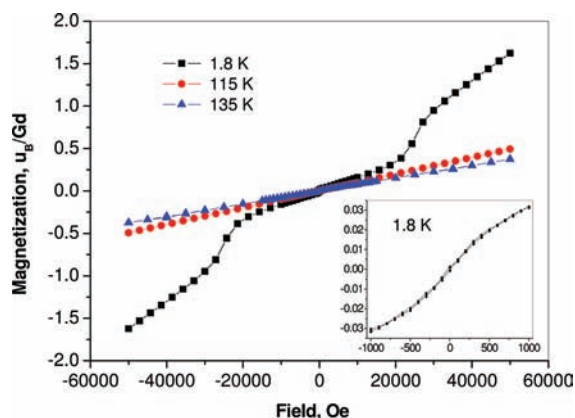


Figure 7. Field dependence of magnetization for $\text{Dy}_5\text{Mg}_5\text{Fe}_4\text{Al}_{12}\text{Si}_6$ at different temperatures.

100 K, and metamagnetic behavior below the Néel temperature. A reorientation of the spins occurs at fields above 20000 G, although saturation is not achieved.

$\text{Dy}_5\text{Mg}_5\text{Fe}_4\text{Al}_{12}\text{Si}_6$ exhibits a sharp antiferromagnetic transition at 6.9 K (Figure 8). In the paramagnetic regime above

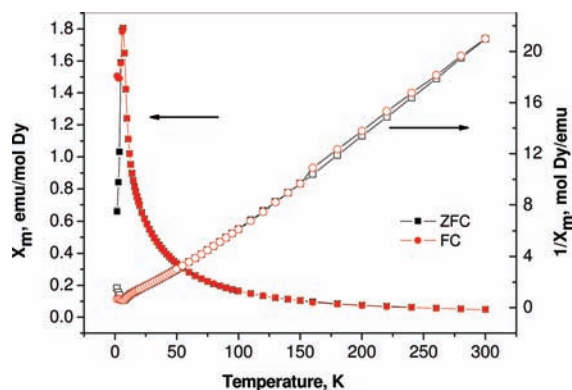


Figure 8. Temperature dependence of magnetic susceptibility of $\text{Dy}_5\text{Mg}_5\text{Fe}_4\text{Al}_{12}\text{Si}_6$ at 100 Oe.

this temperature, the magnetic susceptibility data can be fit to the Curie–Weiss law, indicating an effective moment per Dy^{3+} ion of $10.55 \mu_B$ (close to the expected value of $10.63 \mu_B$)³⁴ and a Weiss constant of 9.9 K. The positive sign of the Weiss constant is indicative of ferromagnetic coupling at high temperatures. The presence of this coupling at high temperatures and the antiferromagnetic transition at low temperature indicates competing magnetic forces, likely caused by the presence of two rare earth crystallographic sites in the unit cell. This is further evidenced by the complexity of the magnetization data below the ordering temperature, which shows several metamagnetic transitions (see Figure 9). A small amount of hysteresis is observed at low fields, possibly indicating that the initial ordering is ferrimagnetic or canted; as the applied field increases, spin reorientations occur at 10000

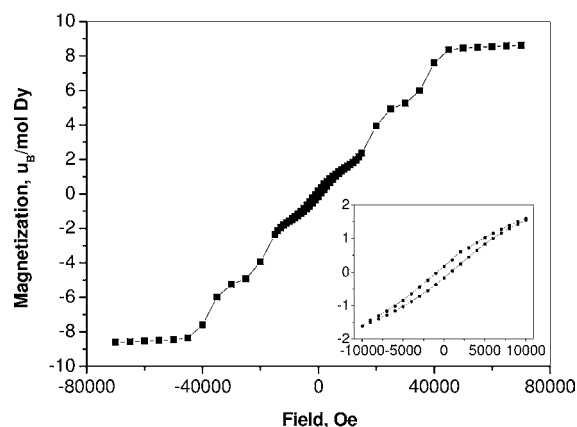


Figure 9. Field dependence of magnetization for $\text{Dy}_5\text{Mg}_5\text{Fe}_4\text{Al}_{12}\text{Si}_6$ at 1.8 K.

G, 20000 G, and 40000 G, achieving saturated ferromagnetic ordering above 40000 G.

CONCLUSION

Reactions of Si, Fe, and R = Gd, Dy, and Y in mixed Mg/Al flux have yielded quinary phases $\text{R}_5\text{Mg}_5\text{Fe}_4\text{Al}_x\text{Si}_{18-x}$ with a new structure type. While structural studies, elemental analysis, and NMR data point to a stoichiometry of $\text{R}_5\text{Mg}_5\text{Fe}_4\text{Al}_{12}\text{Si}_6$, mixing of Al and Si on several sites and concomitant phase width cannot be ruled out. Neutron diffraction studies are planned to confirm the Al and Si siting and to further investigate the nature of the magnetic ordering of the rare earth moments. The $\text{R}_5\text{Mg}_5\text{Fe}_4\text{Al}_{12}\text{Si}_6$ phases exhibit significant charge transfer from the strongly electropositive elements (rare earths and magnesium) to the more electronegative Fe, Al, and Si atoms; however, the compounds are still metallic. Syntheses in the strongly reducing Mg/Al flux appear to be a rich source of complex multinary phases that are close to the metal/semiconducting Zintl phase border.

ASSOCIATED CONTENT

Supporting Information

Elemental analysis data, tables of atomic positions and thermal parameters for Gd and Y analogues, and powder diffraction patterns; and crystallographic data for $\text{R}_5\text{Mg}_5\text{Fe}_4\text{Al}_{12}\text{Si}_6$ (R = Gd, Dy, Y) in the form of CIF files. This material is available free of charge via the Internet at <http://pubs.acs.org>.

AUTHOR INFORMATION

Corresponding Author

*E-mail: latturme@chem.fsu.edu. Phone: 850-644-4074.

Notes

The authors declare no competing financial interest.

ACKNOWLEDGMENTS

This research was supported by funding from the National Science Foundation (Division of Materials Research) through Grants DMR-05-47791 and DMR-11-06150. This work made use of the NMR Facilities of the FSU Chemistry Department.

REFERENCES

- (1) Murarka, S. P. *Intermetallics* **1995**, *3*, 173–186.
- (2) Michel, E. G. *Appl. Surf. Sci.* **1997**, *117/118*, 294–302.
- (3) Tani, J.; Kido, H. *J. Appl. Phys.* **1999**, *86*, 464–467.

- (4) Ai, Y.; Luo, C. P.; Liu, J. *Acta Mater.* **2007**, *55*, 531–538.
- (5) Poole, W. J., Ed.; *Aluminium Alloys 2006, Pts 1 and 2—Research through Innovation and Technology*. *Mater. Sci. Forum* **2006**, *519–521*, 377–382.
- (6) Hosseinifar, M.; Malakhov, D. V. *Metall. Mater. Trans. A* **2011**, *42A*, 825–833.
- (7) Barlock, J. G.; Mondolfo, L. F. *Z. Metallkd.* **1975**, *66*, 605–611.
- (8) Sebastian, C. P.; Malliakas, C. D.; Chondroudi, M.; Schellenberg, I.; Rayaprol, S.; Hoffmann, R. D.; Pöttgen, R.; Kanatzidis, M. G. *Inorg. Chem.* **2010**, *49*, 9574–9580.
- (9) Vojteer, N.; Schroeder, M.; Röhr, C.; Hillebrecht, H. *Chem.—Eur. J.* **2008**, *14*, 7331–7342.
- (10) Roudebush, J. H.; Toberer, E. S.; Hope, H.; Snyder, G. J.; Kauzlarich, S. M. *J. Solid State Chem.* **2011**, *184*, 1176–1185.
- (11) (a) Benbow, E. M.; Dalal, N.; Latturmer, S. E. *J. Am. Chem. Soc.* **2009**, *131*, 3349–3354. (b) Benbow, E. M.; Dalal, N. S.; Latturmer, S. E. *J. Solid State Chem.* **2009**, *182*, 3055–3062.
- (12) Lang, D. A.; Zaikina, J. V.; Lovingood, D. D.; Gedris, T. E.; Latturmer, S. E. *J. Am. Chem. Soc.* **2010**, *132*, 17523–17530.
- (13) Lang, D. A.; Latturmer, S. E. *Eur. J. Inorg. Chem.* **2011**, *26*, 4006–4011.
- (14) Whalen, J. B.; Zaikina, J. V.; Achey, R.; Stillwell, R.; Zhou, H.; Wiebe, C. R.; Latturmer, S. E. *Chem. Mater.* **2010**, *22*, 1846–1853.
- (15) Massalski, T. B.; Okamoto, H. *Binary Alloy Phase Diagrams*, 2nd ed.; ASM International: Materials Park, OH, 1990.
- (16) *SAINT*, Version 6.02a; Bruker AXS, Inc.: Madison, WI, 2000.
- (17) Sheldrick, G.M. *SHELXTL NT/2000*, Version 6.1; Bruker AXS, Inc.: Madison, WI, 2000.
- (18) Villars, P.; Calvert, L. D. *Pearson's Handbook—Crystallographic Data for Intermetallic Phases*; ASM International: Materials Park, OH, 1998.
- (19) (a) Kranenberg, C.; Mewis, A. Z. *Anorg. Allg. Chem.* **2000**, *626*, 1448–1453. (b) Chen, X. Z.; Sieve, B.; Henning, R.; Schultz, A. J.; Brazis, P.; Kannewurf, C. R.; Cowen, J. A.; Crosby, R.; Kanatzidis, M. G. *Angew. Chem., Int. Ed.* **1999**, *38*, 693–696.
- (20) Sieve, B.; Gray, D. L.; Henning, R.; Bakas, T.; Schultz, A. J.; Kanatzidis, M. G. *Chem. Mater.* **2008**, *20*, 6107–6115.
- (21) (a) Krendelsberger, R.; Rogl, P.; Leithe-Jasper, A.; Simensen, C. *J. Alloys Compd.* **1998**, *264*, 236–239. (b) Foss, S.; Olsen, A.; Simensen, C. J.; Taftø, J. *Acta Crystallogr., Sect. B* **2003**, *B59*, 36–42.
- (22) Roger, J.; Bosselet, F.; Viala, J. C. *J. Solid State Chem.* **2011**, *184*, 1120–1128.
- (23) Carter, G. C.; Bennett, L. H.; Kahan, D. J. *Metallic Shifts in NMR*. In *Progress in Materials Science*; Pergamon Press: New York, NY, 1977; Vol. 20.
- (24) Cokoja, M.; Parala, H.; Schroter, M. K.; Birkner, A.; van den Berg, M. W. E.; Gruner, W.; Fischer, R. A. *Chem. Mater.* **2006**, *18*, 1634–1642.
- (25) Baek, S. H.; Suh, B. J.; Pavarini, E.; Borsa, F.; Barnes, R. G.; Bud'ko, S. L.; Canfield, P. C. *Phys. Rev. B* **2002**, *66*, 104510.
- (26) Jehle, M.; Scherer, H.; Wendorff, M.; Röhr, C. *J. Solid State Chem.* **2009**, *182*, 1129–1135.
- (27) (a) Sears, R. E. *J. Phys. Rev. B* **1980**, *22*, 1135. (b) Han, O. H.; Timken, H. K. C.; Oldfield, E. *J. Chem. Phys.* **1988**, *89*, 6046.
- (28) Brauniger, T.; Chandran, C. V.; Wedig, U.; Jansen, M. Z. *Anorg. Allg. Chem.* **2011**, *637*, 530–535.
- (29) Klinowski, J. *Annu. Rev. Mater. Sci.* **1988**, *18*, 189–218.
- (30) Condron, C. L.; Martin, M.; Nolas, G. S.; Piccoli, P. M. B.; Schultz, A. J.; Kauzlarich, S. M. *Inorg. Chem.* **2006**, *45*, 9381–9386.
- (31) Gou, W.; Rodriguez, S. Y.; Li, Y.; Ross, J. H. *Phys. Rev. B* **2009**, *80*, 144108.
- (32) He, J.; Klug, D. D.; Uehara, K.; Preston, K. F.; Ratcliffe, C. I.; Tse, J. S. *J. Phys. Chem. B* **2001**, *105*, 3475–3485.
- (33) Stearns, L. A.; Gryko, J.; Diefenbacher, J.; Ramachandran, G. K.; McMillan, P. F. *J. Solid State Chem.* **2003**, *173*, 251–258.
- (34) Kittel, C. *Introduction to Solid State Physics*, 6th ed.; John Wiley & Sons, Inc.: New York, 1986.